Chapter 3

Hierarchical Control for DC Microgrids

Ahmed Mohamed

Additional information is available at the end of the chapter

http://dx.doi.org/10.5772/63986

Abstract

In this chapter, the design and control of DC microgrids will be discussed. Depending on the time and bandwidth requirements, microgrid controllers can be categorized to primary local controllers (LC) and secondary microgrid central controllers (MGCC). The functions of the two categories of controllers will be presented and explained, using simulations and hardware experiments. In addition, the design of the power electronic converters linking the various resources and loads within the DC microgrid to the common DC bus, as well as the converters used to connect the microgrid to the main grid, will be presented. An example of the interaction of the MGCC with the controller of the main grid will be investigated. This chapter is intended to give a practical overview of the design and control of DC microgrids.

Keywords: control, DC microgrids, inverter, primary microgrid control, secondary microgrid control

1. Introduction

Electric power systems are undergoing profound and radical changes triggered by the imperative to fulfill two objectives: (1) increase the power system resilience and (2) combat global warming. Resilience, as articulated by the Presidential Policy Directive 21 [1], refers to "the ability to withstand and recover from deliberate attacks, accidents, or naturally occurring threats or incidents." In order to approach the *first* objective, consumers must be equipped with generators and storage elements in order to supply their loads locally during blackouts. In other words, the bulk power system will be divided into many local energy networks, namely microgrids, which are interconnected through the main power network during

normal operating conditions, but can island themselves and operate independently when a fault occurs. Microgrids increase the overall efficiency of the system by satisfying part of their load locally, reducing the amount of power imported over long transmission lines. The effort to achieve the *second* objective is aided by increasing renewable energy generation. There is a wide consensus that if we are to realize the full environmental, societal, and economic benefits of microgrid deployment, while also improving resilience, microgrids must be based on renewable energy.

According to the U.S. Department of Energy, a microgrid is "a group of interconnected loads and distributed energy resources (DERs) with clearly defined electrical boundaries that acts as a single controllable entity with respect to the electric utility grid." A microgrid can be connected to the grid, in a grid-connected mode, or independent from the grid, in an islanded mode. Operation and control of microgrids have been given genuine attention in the literature. Each of the individual resources and controllable loads needs a controller. These controllers are referred to as local or resource controllers. In addition, a microgrid central controller (MGCC) is needed to act as a coordinator/supervisor to the local controllers (LCs).

The speed and bandwidth requirements significantly vary between LCs and MGCCs. LCs need to be faster since they have to deal with current and voltage commands and measurements, whereas MGCCs take a supervisory role in managing the power flow of the assets and loads within the microgrid and between the microgrid and the main grid. In addition, MGCCs fix any errors, for example, frequency deviation that may result from primary control [2, 3]. Tertiary control of microgrids refers the layer of control that extends beyond the boundaries of a single microgrid. It coordinates the interaction between various microgrids in close vicinity and the main grid. A virtual power plant whether owned by the utility company or a third party, aggregating some microgrids in a given geographic area, can be considered an example of tertiary control. This layer of control is typically considered as a part of the main grid's control [2, 4] and will be out of the scope of this chapter. However, by the end of the chapter, the interaction of the MGCC with the main grid will be highlighted.

DC microgrids offer several advantages over AC microgrids [5, 6]. Electronic devices, such as computers, routers, and electronic lights (either fluorescent or LED), represent a high percent of the electric load in many buildings today. Moreover, variable speed drives (VFD) are increasingly used for electric motors. A DC environment is found to be a more convenient way to deliver power to these loads to assure reliability and redundancy. DC networks do not need AC to DC conversion for every electronic device, which has a significant impact on the efficiency. DC can reduce the losses associated with switch-mode supplies and uninterruptible power supplies. Furthermore, incorporating DC microgrids has the benefit of superior compatibility of the DC power with renewable energy generators, for example, photovoltaics (PV), electric vehicles, and energy storage systems (ESSs) [7–10].

In this chapter, we will focus on the design of primary and secondary control techniques for DC microgrids. Computer simulations and hardware testing will be used to verify the presented techniques. The simulation results were obtained using MATLAB/Simulink and the SimPowerSystems sublibrary.

http://dx.doi.org/10.5772/63986

2. Microgrid structure

The DC microgrid under study is assumed to be dependent mainly on the sustainable energy sources, as shown in **Figure 1**. The microgrid is connected to the main grid, so that it can operate in a grid-connected mode. Moreover, it includes an ESS, so that it can operate in an islanded mode during blackout/brownout conditions. During the grid-connected mode, power can be drawn either from the main grid or from the ESS in case the locally generated renewable energy is not enough to satisfy the load demand.

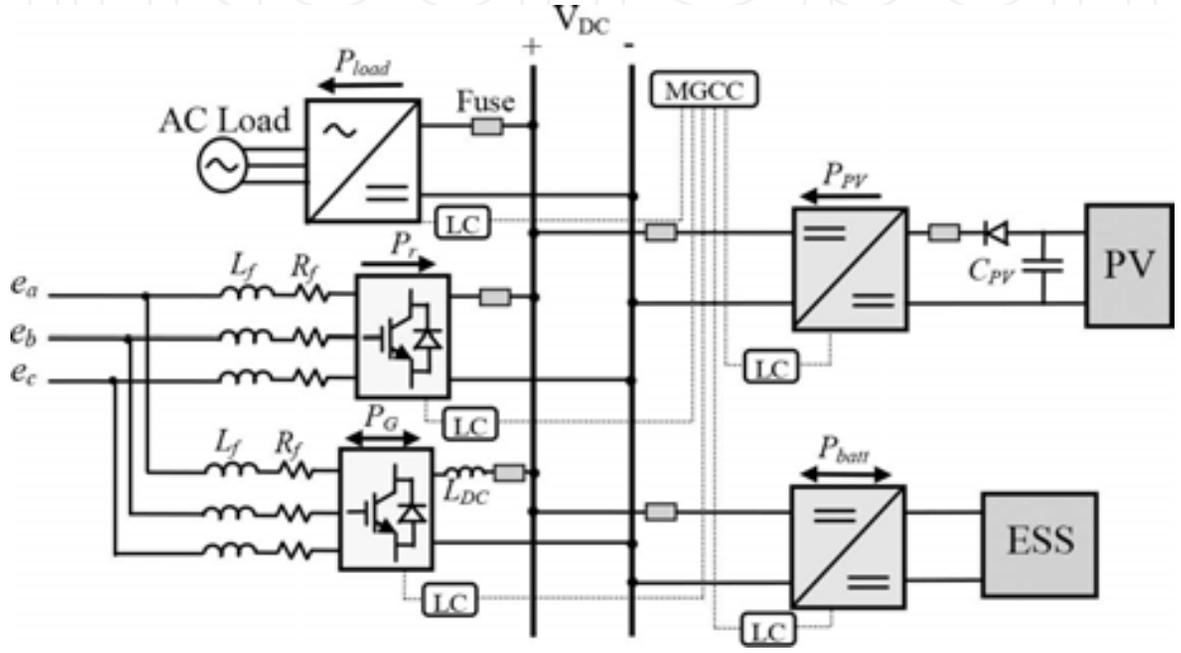

Figure 1. DC microgrid architecture and control hierarchy.

Since the microgrid is based on renewable energy, certain features had to be maintained to assure efficient integration of the renewable resources, such as efficient and reliable load-feeding capability and full controllability of voltage and power flow among the various buses in the system. The connectivity of the DC microgrid to the main grid should allow voltage regulation on the DC side. Furthermore, it should allow bidirectional power flow between AC and DC sides, depending on the desired mode of operation.

Specifically, a fully controlled rectifier was used to tie the DC network to the AC grid while working at unity power factor. This rectifier is dedicated to regulating the voltage on the DC bus in the grid-connected mode. Therefore, it enables unidirectional power flow from the main grid to the DC microgrid. Alternatively, one of the other resource converters, for example, the bidirectional battery charger, must be responsible for regulating the DC bus voltage. A fully controlled bidirectional AC–DC converter was used to control the active/reactive power exchange with the main grid. It employs a vector decoupling control technique, which enables independent control of the active and reactive power in both directions. Each converter is controlled via a LC. A MGCC communicates with the LCs and coordinates their operation.

3. Energy link integration

3.1. Converters and control design

The ESS and PV will be linked to the common DC bus of the microgrid through DC–DC converters. Boost converter is commonly used to interface renewable energy sources yielding DC voltage to the DC microgrid. In case of PV systems, a controlled boost converter shall serve two functionalities: (1) it steps up the output voltage of the PV system to be compatible with the DC bus voltage and (2) it regulates the output voltage or power, for example, corresponding to a predefined maximum power point tracking algorithm. The boost converter topology may be slightly modified when used as an interface for PV systems in a DC microgrid. For instance, since the DC bus may already possess high capacitance (i.e., owing to the other converters connected to the same bus), the boost converter capacitor can be omitted, resulting in a discontinuous instantaneous output current. A solution to maintain continuous output current is to synchronize multiple DC–DC converters (i.e., interleaved converters) [11, 12].

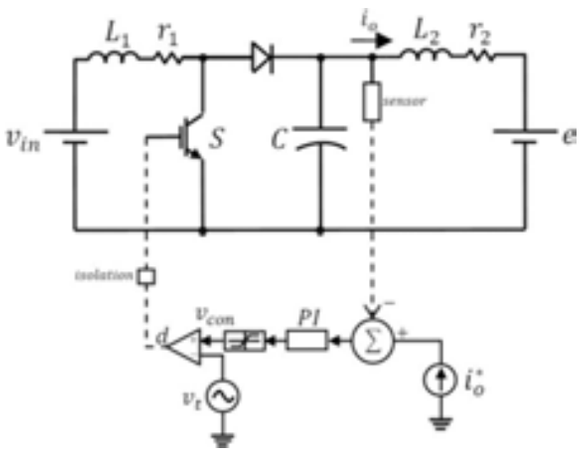

Figure 2. The proposed inductively coupled boost converter topology for fuel cells integration into a DC ZEDS.

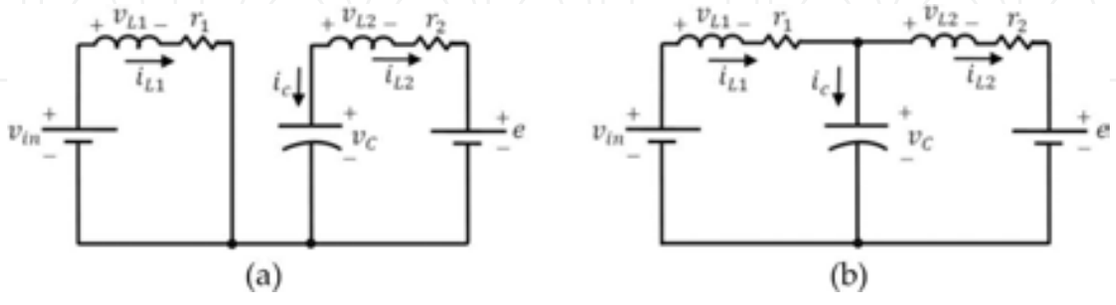

Figure 3. The ON and OFF states of the DC–DC converter with output L-filter: (a) ($0 < t \leq DTs$) and (b) ($DTs < t \leq T$).

Another approach to solve the problem of discontinuity in the output current is by adding an L-filter to the output side of the converter, as shown in **Figure 2**. The added inductance assures

continuous conduction of the output current. The configurations of the circuit during the ON and OFF states of the switches are shown in **Figure 3**, where the parameter D in the caption refers to the duty cycle and T_s refers to the switching time.

The small-signal mathematical model of this converter can be obtained using the state-space averaging technique. The state-space model during the interval ($0 < t \le DT_s$) is [11]

$$\begin{bmatrix} \dot{i}_{L1} \\ \dot{i}_{L2} \\ \dot{v}_c \end{bmatrix} = \begin{bmatrix} \frac{-r_1}{L_1} & 0 & \frac{-1}{L_1} \\ 0 & \frac{-r_2}{L_2} & \frac{1}{L_2} \\ 0 & \frac{-1}{C} & 0 \end{bmatrix} \begin{bmatrix} i_{L1} \\ i_{L2} \\ v_C \end{bmatrix} + \begin{bmatrix} \frac{1}{L_1} & 0 \\ 0 & \frac{-1}{L_2} \\ 0 & 0 \end{bmatrix} \begin{bmatrix} v_{in} \\ e \end{bmatrix} \tag{1}$$

whereas the state-space model during the interval ($DT_s < t \le T$) is

$$\begin{bmatrix} \dot{i}_{L1} \\ \dot{i}_{L2} \\ \dot{v}_c \end{bmatrix} = \begin{bmatrix} \frac{-r_1}{L_1} & 0 & 0 \\ 0 & \frac{-r_2}{L_2} & \frac{1}{L_2} \\ \frac{1}{C} & \frac{-1}{C} & 0 \end{bmatrix} \begin{bmatrix} i_{L1} \\ i_{L2} \\ v_C \end{bmatrix} + \begin{bmatrix} \frac{1}{L_1} & 0 \\ 0 & \frac{-1}{L_2} \\ 0 & 0 \end{bmatrix} \begin{bmatrix} v_{in} \\ e \end{bmatrix} \tag{2}$$

$$i_0 = i_{L2} \tag{3}$$

Using the state-space averaging technique,

$$\begin{bmatrix} \langle \dot{i}_{L1} \rangle \\ \langle \dot{i}_{L2} \rangle \\ \langle \dot{v}_c \rangle \end{bmatrix} = \begin{bmatrix} \frac{-r_1}{L_1} & 0 & \frac{-d}{L_1} \\ 0 & \frac{-r_2}{L_2} & \frac{1}{L_2} \\ \frac{(1-d)}{C} & \frac{-1}{C} & 0 \end{bmatrix} \begin{bmatrix} \langle i_{L1} \rangle \\ \langle i_{L2} \rangle \\ \langle v_c \rangle \end{bmatrix} + \begin{bmatrix} \frac{1}{L_1} & 0 \\ 0 & \frac{-1}{L_2} \\ 0 & 0 \end{bmatrix} \begin{bmatrix} \langle v_{in} \rangle \\ \langle e \rangle \end{bmatrix} \tag{4}$$

If we consider a small-signal perturbation, the large-signal state-space equations will be

$$\begin{bmatrix}0\\0\\0\end{bmatrix}=\begin{bmatrix}\frac{-r_1}{L_1} & 0 & \frac{-d}{L_1}\\ 0 & \frac{-r_2}{L_2} & \frac{1}{L_2}\\ \frac{(1-d)}{C} & \frac{-1}{C} & 0\end{bmatrix}\begin{bmatrix}I_{L1}\\I_{L2}\\V_c\end{bmatrix}+\begin{bmatrix}\frac{1}{L_1} & 0\\ 0 & \frac{-1}{L_2}\\ 0 & 0\end{bmatrix}\begin{bmatrix}V_{in}\\E\end{bmatrix} \tag{5}$$

whereas the small-signal state-space set of equations will be

$$\begin{bmatrix}\hat{i}_{L1}\\\hat{i}_{L2}\\\hat{v}_c\end{bmatrix}=\begin{bmatrix}\frac{-r_1}{L_1} & 0 & \frac{-D}{L_1}\\ 0 & \frac{-r_2}{L_2} & \frac{1}{L_2}\\ \frac{(1-D)}{C} & \frac{-1}{C} & 0\end{bmatrix}\begin{bmatrix}\hat{i}_{L1}\\\hat{i}_{L2}\\\hat{v}_c\end{bmatrix}+\begin{bmatrix}\frac{1}{L_1} & \frac{-V_c}{L_1}\\ 0 & 0\\ 0 & \frac{-I_{L1}}{C}\end{bmatrix}\begin{bmatrix}\hat{v}_{in}\\\hat{d}\end{bmatrix} \tag{6}$$

where

$$i_{L1}=I_{L1}+\hat{i}_{L1},\ i_{L2}=I_{L2}+\hat{i}_{L2},\ v_c=V_c+\hat{v}_c,\ v_{in}=V_{in}+\hat{v}_{in},\ e=E+\hat{e},\ d=D+\hat{d}$$

3.2. Energy link integration results and discussion

A prototype system was designed and implemented in hardware to examine the performance of the inductively coupled boost converter. The set of equations described in Section 3.1 was

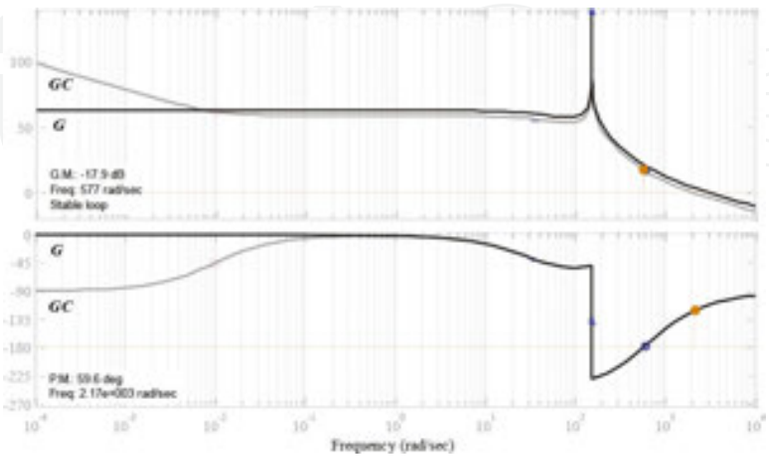

Figure 4. Bode plots of the developed controller.

used to design a closed-loop proportional-Integral (PI) controller. The digital signal processing board dSPACE 1104 was used to control the converter in real time. The switching frequency for the converter was 5 kHz. The parameters of the implemented converter prototype were as follows: L_1 is 2.2 mH, L_2 is 24 mH, r_1 is 0.06 ohm, r_2 is 0.84 ohm, and C is 4800 μf. The Bode plots of the open-loop and closed-loop responses for the developed controller are given in **Figure 4**.

Results for the inductively coupled boost converter are shown in **Figure 5**. The output current reference changed from 1 to 3 A after 5 s. It can be seen that the output current is continuous, and the ripple is as small as 2%, which means a high power quality injected to the DC microgrid.

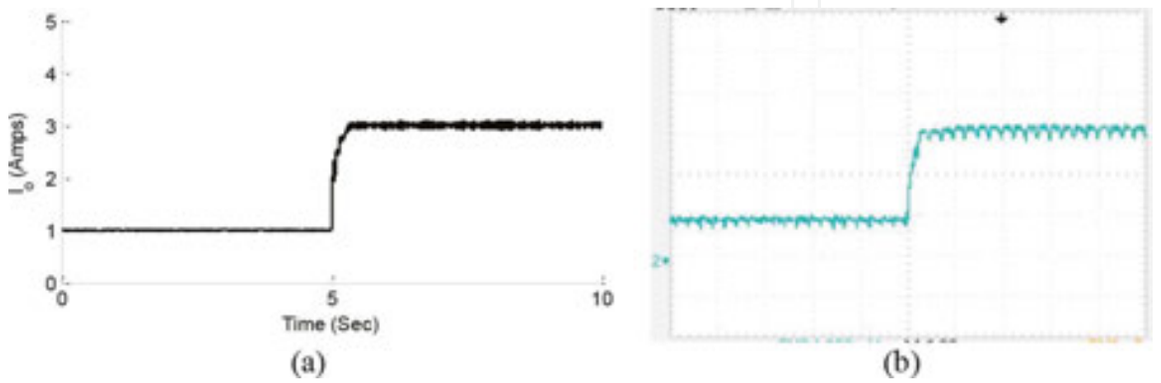

Figure 5. Results for (inductively coupled boost converter): (a) simulation results and (b) experimental results (the same scale: 1 A/division).

4. Microgrid to main grid connectivity

4.1. DC bus voltage regulation

4.1.1. Converter description and mathematical modeling

A fully controlled three-phase rectifier will be used for coupling the DC network to the AC grid. In our case study, we designed and implemented the rectifier such that it regulates the voltage of the DC bus, while being able to operate at unity power factor. This was achieved through a vector decoupling control technique and sinusoidal pulse width modulation (SPWM).

Vector decoupling SPWM control is based on converting the voltages and currents from the three-phase abc frame of references to the d–q frame of references. Even though mathematical models for the system have been derived, PI controllers were implemented to control the rectifier rather than model-based control due to its relative simplicity and effectiveness. However, the mathematical models play an important role in decoupling the vectors, which is essential to achieve independent P/Q control. The three-phase SPWM rectifier circuit and its single-phase equivalent are shown in **Figure 6** [13].

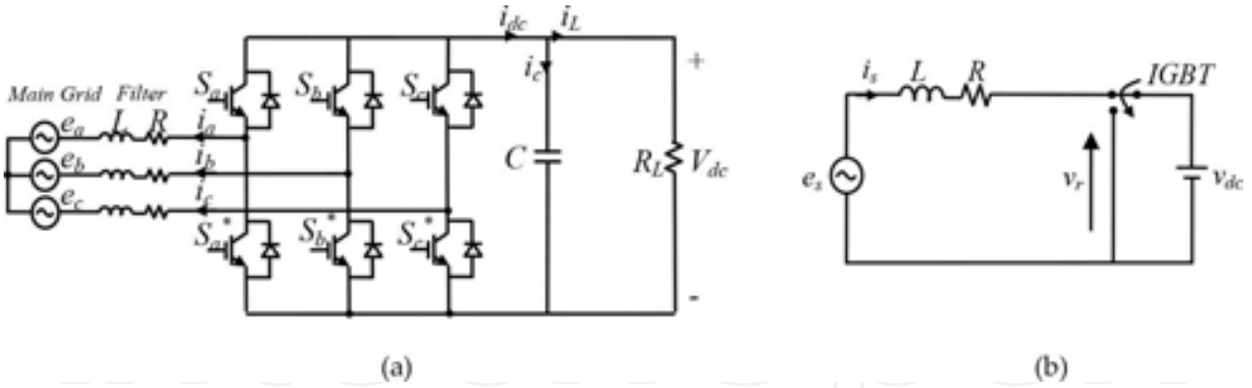

Figure 6. The implemented three-phase SPWM rectifier: (a) circuit diagram and (b) single-phase equivalent.

The voltage equation is

$$e_s = Ri_s + L\frac{di_s}{dt} + v_r \tag{7}$$

where

e_s is the source voltage

i_s is the source current

v_r is the converter input voltage

R, *L* Resistance and inductance of the boosting inductor, respectively.

$$L\frac{di_{de}}{dt} - wLi_{qe} + Ri_{de} = e_{de} - v_{de} \tag{8}$$

$$L\frac{di_{qe}}{dt} - wLi_{de} + Ri_{qe} = e_{qe} - v_{qe} \tag{9}$$

where w is the angular frequency of the voltage source in radians.

The rectifier should instantaneously draw enough input power to satisfy the sum of the load demand and the charging rate of the capacitor energy, to maintain fast voltage control. Neglecting the thermal and switching device losses, the power balance between the AC input and the DC output is as follows:

$$P = \frac{3}{2}\left(e_{de}i_{de} + e_{qe}i_{qe}\right) = v_{dc}i_{dc} \tag{10}$$

where v_{dc} and i_{dc} are the DC output voltage and current, respectively.

On the DC output side,

$$i_{dc} = -C\frac{dv_{dc}}{dt} - i_L \tag{11}$$

where i_L is the load current. From Eqs. (10) and (11),

$$\frac{3}{2}(e_{de}i_{de} + e_{qe}i_{qe}) = -Cv_{dc}\frac{dv_{dc}}{dt} - v_{dc}i_L \tag{12}$$

Inspecting Eq. (12), we can see that the system is nonlinear with regard to v_{dc}. From Eqs. (8), (9), and (11), a complete state-space modeling of the system is given by

$$\begin{bmatrix} \dot{i}_{de} \\ \dot{i}_{qe} \\ \dot{v}_{dc} \end{bmatrix} = \begin{bmatrix} -\frac{R}{L}i_{de} - wi_{qe} \\ -\frac{R}{L}i_{qe} + wi_{de} \\ -\frac{3}{2Cv_{DC}}(e_{de}i_{de} + e_{qe}i_{qe}) + \frac{i_L}{C} \end{bmatrix} + \begin{bmatrix} \frac{1}{L} & 0 \\ 0 & \frac{1}{L} \\ 0 & 0 \end{bmatrix} \begin{bmatrix} e_{de} - v_{de} \\ e_{qe} - v_{qe} \end{bmatrix} \tag{13}$$

4.1.2. Vector decoupling technique

Two nested loops including three PI controllers were implemented to achieve DC voltage as well as input current control. The outer loop is for controlling the DC bus voltage, while the inner loop is for current control. Due to the vector transformation from abc to d–q frame of references, the controller deals with three DC signals, which help eliminate steady-state errors in the developed PI controllers.

In order to completely decouple the d and q components and achieve independent P and Q control, the decoupling terms (wLi_{de}) and (wLi_{qe}) were included while calculating the rectifier's input voltages for V_{rq}^{cont} and, V_{rq}^{cont} respectively. These voltages are the modulation signals for the SPWM technique. The equations used in building the controller are given by Eq. (14):

$$\begin{aligned} v_{rq}^{cont} &= wLi_{de} + e_{qe} - Ri_{qe} - K_p.[i_{de}^{ref} - i_{de}] - K_i.\int[i_{de}^{ref} - i_{de}]dt \\ v_{rd}^{cont} &= -wLi_{qe} - Ri_{qe} - K_p.[i_{de}^{ref} - i_{de}] - K_i.\int[i_{de}^{ref} - i_{de}]dt \end{aligned} \tag{14}$$

In **Figure 7**, a layout for the developed controller is shown.

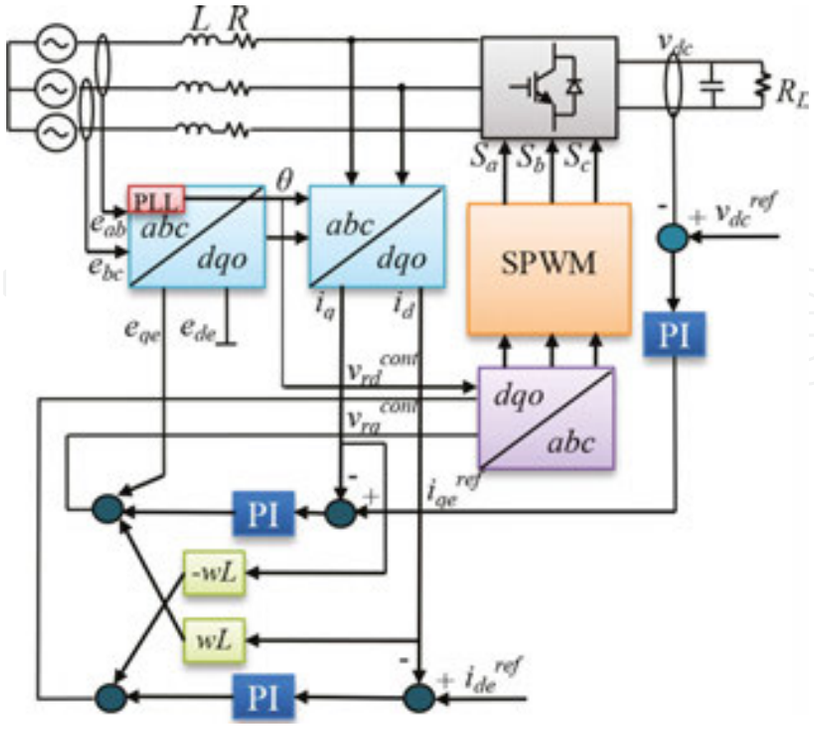

Figure 7. A block diagram of the vector decoupling control implemented on the controlled rectifier.

The controller has the capability to control the active and reactive power independently, and hence, it can be easily set up to operate at unity power factor by adjusting the desired i_{de} to zero. In mathematical terms, this is represented in Eqs. (15) and (16) as follows [13]:

$$P(t) = \frac{3}{2}[e_{qe}(t).i_{qe}(t) + e_{de}(t).i_{de}(t)] \tag{15}$$

$$Q(t) = \frac{3}{2}[e_{de}(t).i_{qe}(t) - e_{qe}(t)i_{de}(t)] \tag{16}$$

4.2. Bidirectional energy transfer

DC microgrids may draw or inject power to the grid, depending on the local generation/demand ratio. Therefore, a bidirectional converter must be put in place to enable such energy transfer. For instance, during times of surplus energy, that is, when power from the PV system is greater than the local load, the power can be injected to the grid if the price for electricity is high and/or the battery is fully charged. On the other hand, power may be drawn by the DC microgrid to cover load deficiencies. The vector decoupling control technique discussed earlier in this chapter was utilized here to enable independent active and reactive power control. For the bidirectional converter, the topology is modified by adding an L-filter (L) on the DC side, as shown in **Figure 8**. Moreover, the DC voltage controller in **Figure 7** is replaced by a current controller, as shown in **Figure 9** [14].

http://dx.doi.org/10.5772/63986

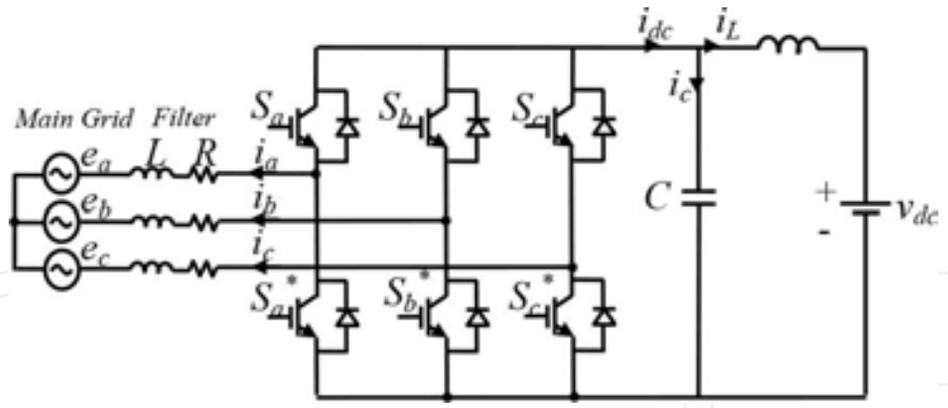

Figure 8. Circuit diagram of the implemented three-phase bidirectional AC–DC/DC–AC converter.

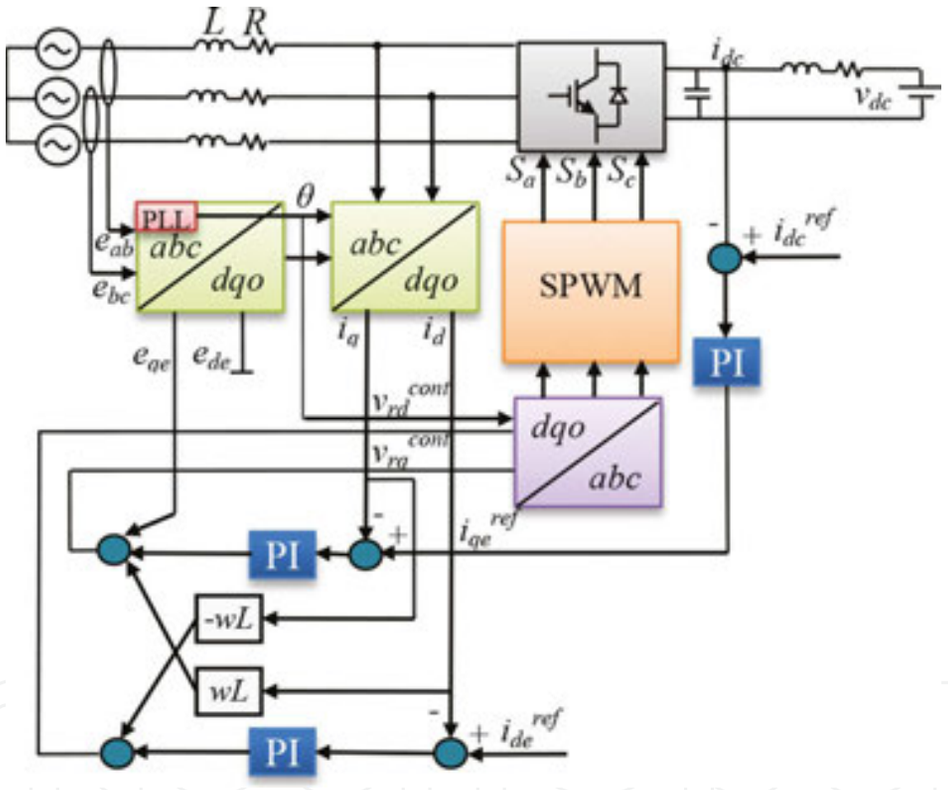

Figure 9. A block diagram of the vector decoupling control implemented on the bidirectional converter.

This controller may be looked at as a means to control the voltage across the L-filter inductor. Corresponding to any given i_{DC}^{ref} value, the controller adjusts the phase of the modulating SPWM signals for the switching devices, until the desired amount of transferred power is achieved. The DC current is positive when the power flows from the main grid to the microgrid, and vice versa. Therefore, the sign of i_{qe}^{ref} determines the mode of operation for the bidirectional converter such that it is in the rectifier mode when the sign is positive, and the inverter mode when it is negative. In both modes of operation, the controller allows independent Q control,

including unity power factor operation by setting i_{de}^{ref}, which is responsible for the reactive power, to zero.

4.3. Grid connectivity results and discussion

Both the unidirectional converter (i.e., the controlled rectifier used for DC bus voltage regulation) and the bidirectional converter were implemented in hardware and simulated in MATLAB/Simulink. The switching frequency for both the converters was 8.04 kHz, and the sampling time was 0.3 ms. Voltage and current sensors were deployed to receive feedback from the various nodes of the system [14]. Several experiments were conducted to test the response of the converters under steady state as well as transient operating conditions. The hardware and simulation results will be presented for the various case studies.

4.3.1. Steady-state performance

The first experiment aimed at testing the steady-state response of the rectifier while operating at unity power factor. Results of this experiment are shown in **Figure 10**. As can be seen in the figure, the current and voltage waveforms are in phase, and the DC bus voltage is regulated at 300 V. The DC current is positive, which according to our notation, means that the power is flowing from the main grid to the DC microgrid.

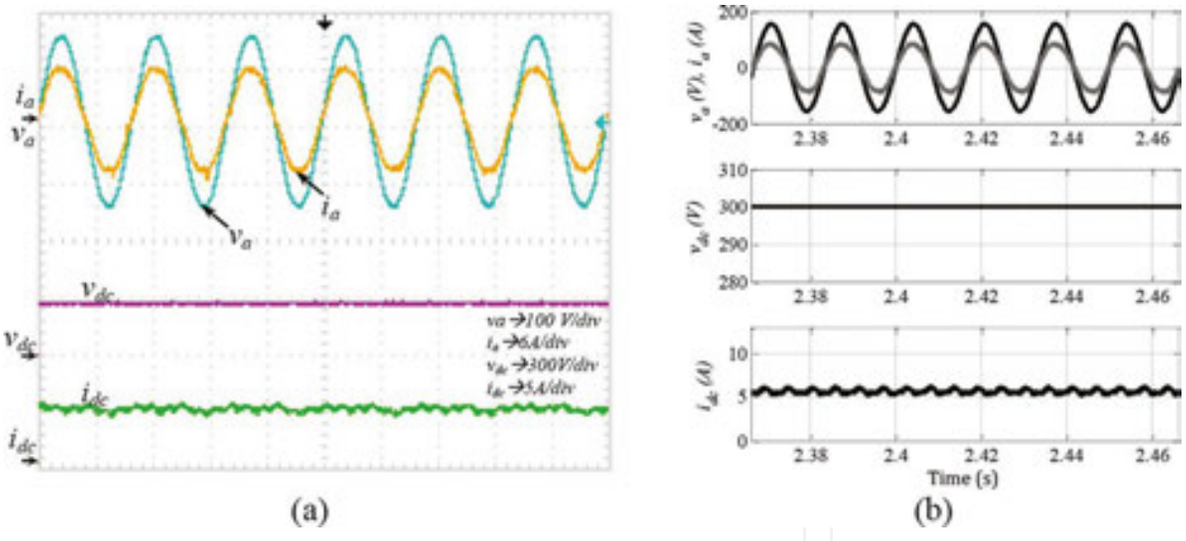

Figure 10. Unity power factor operation of the controlled rectifier: (a) experimental results and (b) simulation results (AC current factorized by 10).

4.3.2. Transient performance

Two experiments were conducted to examine the performance of the developed rectifier under transient operating conditions, namely (1) a step change in the load demand and (2) a step change in the DC microgrid voltage. **Figures 11** and **12** depict the results for these two experiments, respectively.

http://dx.doi.org/10.5772/63986

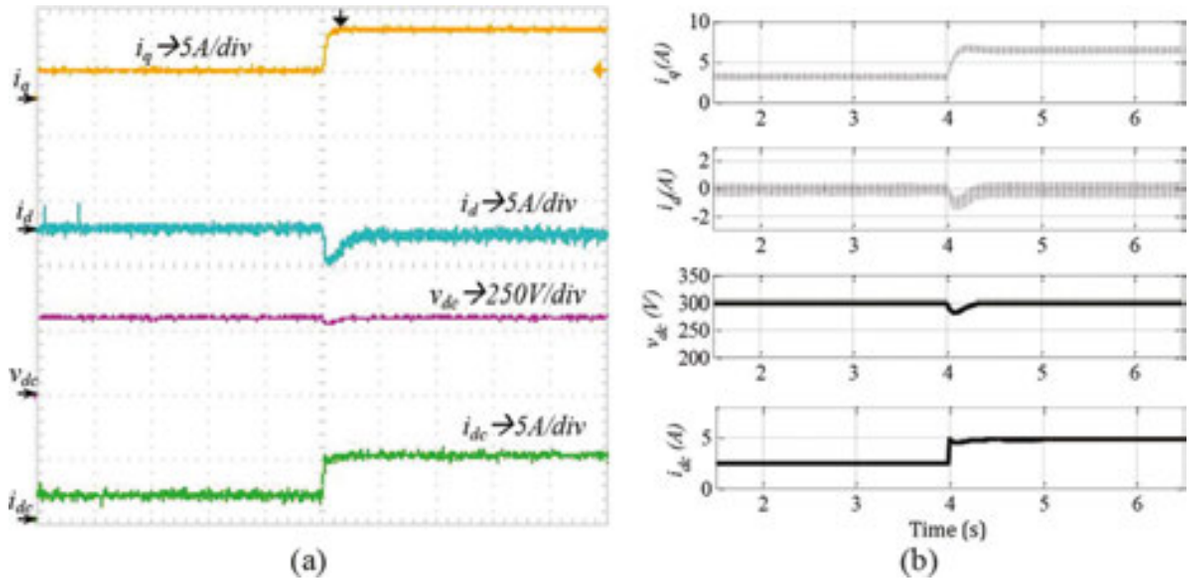

Figure 11. Controlled rectifier's response to a load step change: (a) experimental results and (b) simulation results.

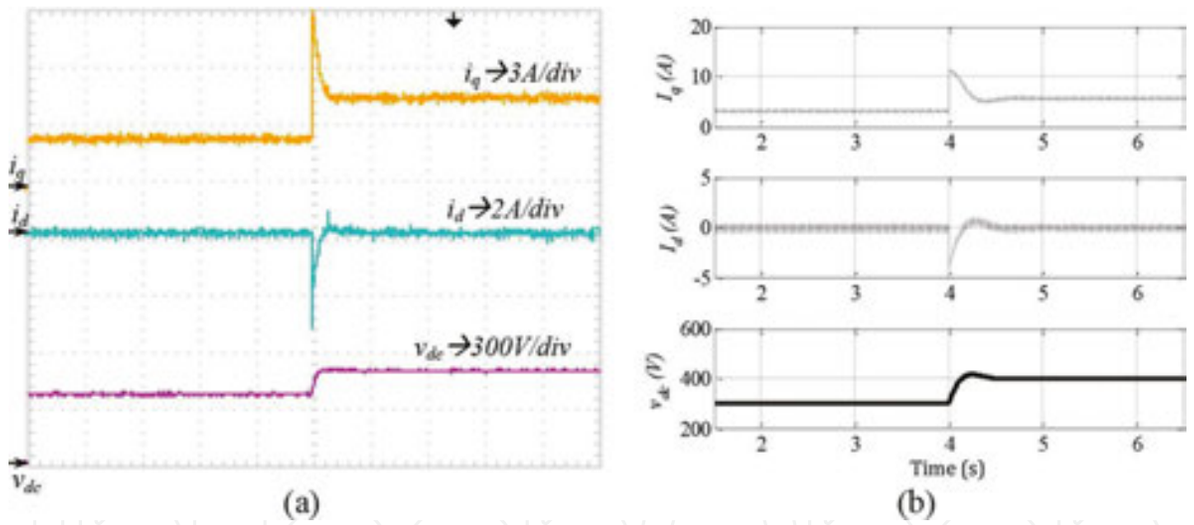

Figure 12. Controlled rectifier's response to a change in the output voltage: (a) experimental results and (b) simulation results.

For the first experiment, whose results are shown in **Figure 11**, the DC load was suddenly changed from 0.72 to 1.5 kW. The results show that the converter is capable of responding to the change in the load by increasing the value of i_q. Moreover, it maintains unity power factor operation, since the value of i_d, which is responsible for reactive power, decays back to zero shortly after the load step change. The DC voltage encounters a small undershoot because of the load change, while the DC current increases to satisfy the load.

In the second experiment, v_{DC}^{ref} was increased to represent a sudden change in the DC bus voltage. The rectifier reaches the new voltage set point in ~200 ms. The value of active power

drawn from the grid increases to satisfy the increase in active power demand on the DC microgrid, which is caused by the increased DC voltage. The converter achieves the required voltage by automatically increasing i_q, as shown in **Figure 12**. Meanwhile, i_d encounters some transient conditions but returns to zero to maintain unity power factor operation.

4.3.3. Bidirectional power flow results

The bidirectional converter was implemented using an L-filter value of 24 mH. This filter, which encompasses 0.9 ohm internal resistance, was used to improve the overall total harmonic distortion of the converter and achieve smooth current control. Several experiments were conducted to test the response of the converter under several step changes in the desired power and its direction.

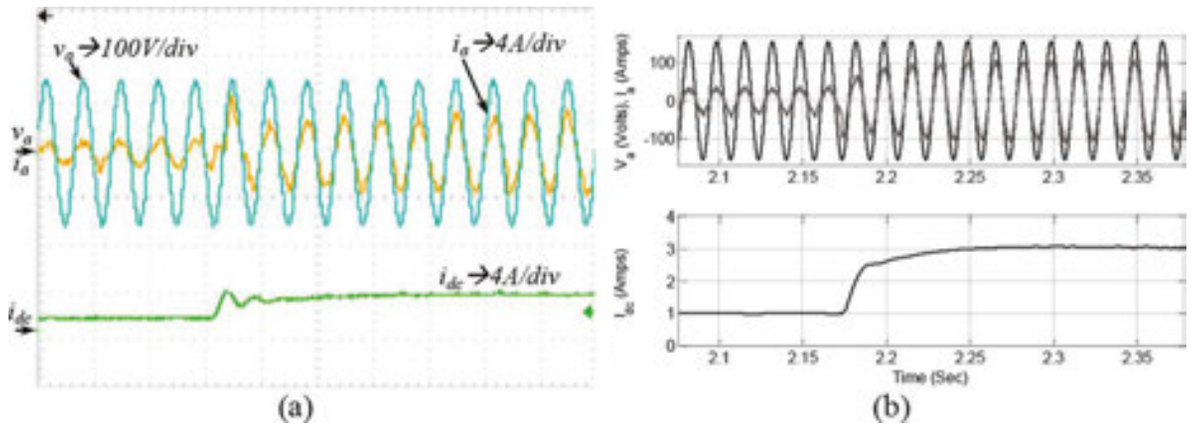

Figure 13. Controlled bidirectional response to DC current reference change from 1 to 3 A: (a) experimental results and (b) simulation results (AC current factorized by 10).

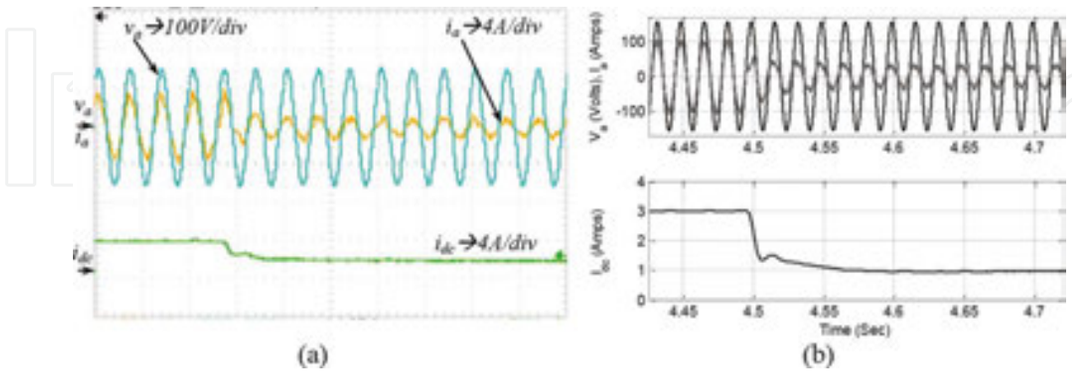

Figure 14. Controlled bidirectional converter response to DC current reference change from 3 to 1 A: (a) experimental results and (b) simulation results (AC current factorized by 10).

The first experiment (see **Figure 13**) involved a step change in the reference current from 1 to 3 A, while operating in the rectifier mode (i.e., the power flows from the main grid to the DC

microgrid). Inspecting **Figure 13**, it can be seen that the converter succeeds in corresponding to the step change in the current reference within a few cycles. The results of a reverse experiment, in which the current reference was decreased from 3 to 1 A, are shown in **Figure 14**. Both experiments verify the applicability of the developed converter. It is worth mentioning that the experimental results match the simulation results. This assures the credibility of the simulation model, which can be used for analyses that may not be easily performed experimentally, for example, fault analysis.

To examine the converter in the inverter mode, the current reference was changed from −3 to −1 A. The negative sign refers to the inverter mode of operation. **Figure 15** shows the results for this experiment. It can be seen that the converter achieves the desired output current, and that the AC current and voltage waveforms are 180° out-of-phase corresponding to the negative active power direction and zero reactive power.

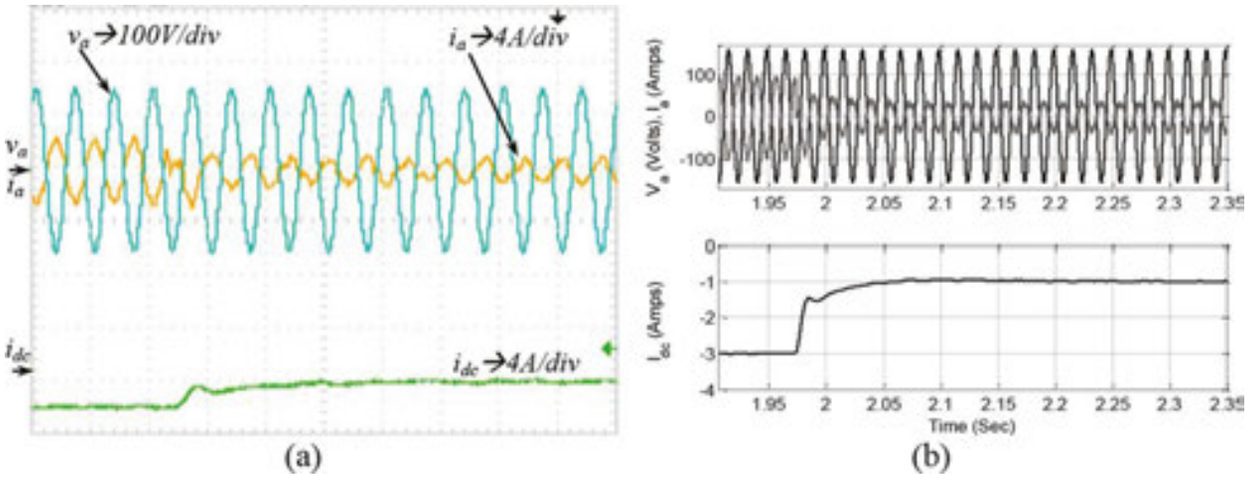

Figure 15. Controlled bidirectional converter response to DC current reference change (−3 to −1 A): (a) experimental results and (b) simulation results (AC current factorized by 10).

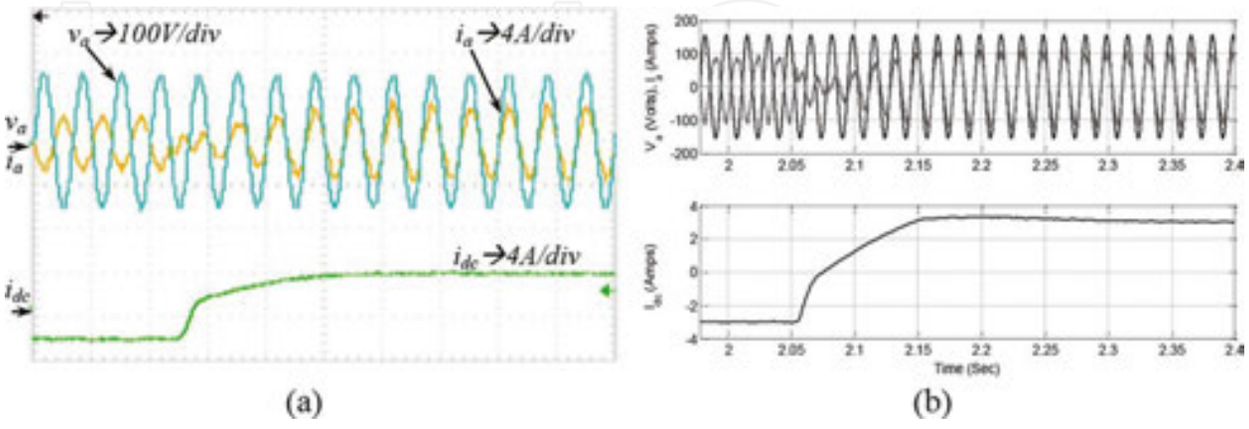

Figure 16. Controlled bidirectional response to DC current reference change (−3 to 3 A): (a) experimental results and (b) simulation results (AC current factorized by 10).

In the developed bidirectional converter, the power can flow in both directions, that is, from AC to DC or from DC to AC. Two experiments were conducted to test the ability of the converter to change the direction of the power instantaneously, while maintaining unity power factor operation. **Figure 16** shows the results of an experiment in which the current reference was changed from −3 to 3 A. This means that the current was flowing from the DC microgrid to the main grid and suddenly reversed its direction. The simulation and experimental results show that the converter was able to control the current and achieve the required step change. **Figure 17** shows the case when the current reference was changed from 3 to −3 A. The results of both experiments show that the converter can smoothly change its mode of operation, from the rectifier to the inverter mode, and vice versa.

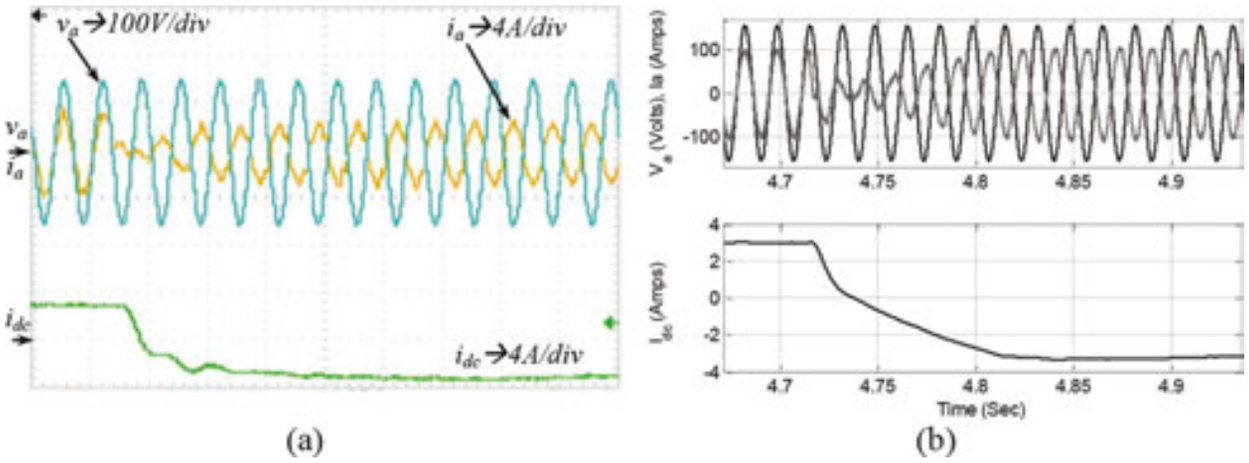

Figure 17. Controlled bidirectional converter response to DC current reference change (3 to −3 A): (a) experimental results and (b) simulation results (AC current factorized by 10).

5. Microgrid central control

The MGCC communicates not only with the LCs to coordinate their operation but also with the controller of the main grid. The main function of the LC is local voltage and current control of the converter that they are associated with. The functions of the secondary controller are optimal microgrid control, for example, energy cost minimization, broadcasting active and reactive power set points, and islanding detection and operation [2, 15, 16].

In order to examine the operation of MGCC, an experiment was conducted. Four AC generators were used to form an AC network. The generators were interconnected through transmission line models. The DC microgrid described earlier within this chapter was connected to the main AC grid at the AC point of common coupling (PCC), as shown in **Figure 18**. The DC microgrid has the ability to draw or inject P and Q to and from the grid. In this experiment, the DC microgrid was regulating the voltage at the PCC. A unity power factor load of 0.7 kW was initially connected to the PCC, as shown in **Figure 19**. The DC microgrid was commanded to receive 100 W and 0 Vars. The AC grid satisfied both the AC load and DC microgrid

demands. The steady-state voltage at PCC was 0.94 pu, while the voltage on the DC bus was 1 pu. After 20 s, following this initial state, the DC microgrid MGCC received a request from the main grid to inject the total amount of demanded power on the AC side [17]. Consequently, the voltage improved to 1.02 pu. The controlled rectifier regulating the voltage on the DC bus maintains a voltage of 1 pu after a transient period of around 6 s with an overshoot of 0.02 pu.

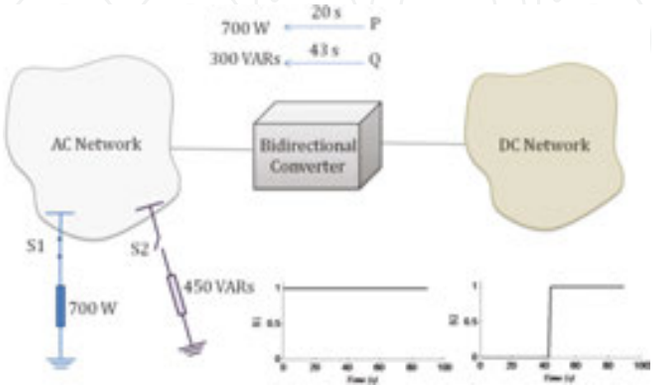

Figure 18. MGCC interaction with the main grid's controller.

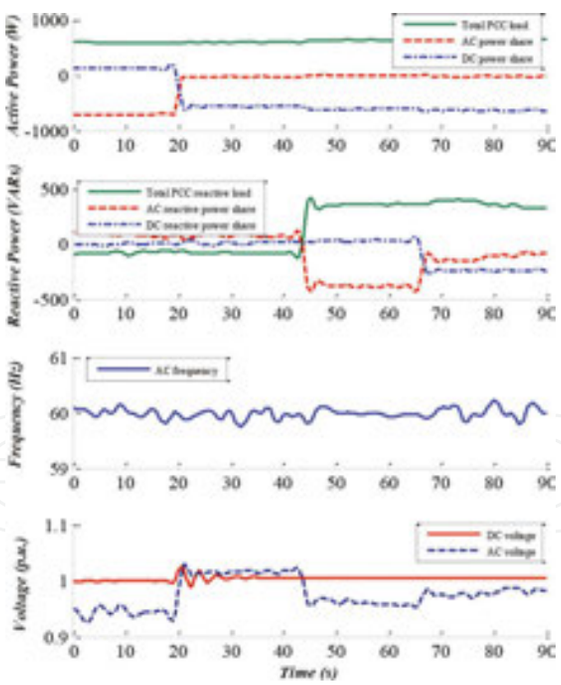

Figure 19. Response of the DC microgrid in an integrated hybrid AC/DC system corresponding to step changes in the load demand reference: (a) the load, DC, and AC active power share; (b) the load, DC, and AC reactive power share; (c) the frequency of the AC bus; and (d) the voltage of the AC and DC buses.

When a reactive load of 0.45 kVARs with lagging power factor is added to the PCC after 43 s, the voltage drops to around 0.95 pu. The DC microgrid is then requested by the main grid to

inject 0.3 kVARs. Therefore, the voltage at the PCC increases to 0.98 pu. The DC bus voltage is hardly affected by this change in its reactive power reference. A maximum of 0.2 Hz frequency deviation was reported, as shown in **Figure 19**. This experiment highlights the coordination that can be achieved between the main grid's controller and the MGCC to enhance the overall performance of the whole system [18].

Author details

Ahmed Mohamed

Address all correspondence to: amohamed@ccny.cuny.edu

Smart Grid Laboratory, Department of Electrical Engineering, City College of the City University of New York, USA

References

[1] The White House, Washington. Presidential Policy Directive 21: Critical Infrastructure Security and Resilience (PPD-21) [Internet]. Feb. 2013. Available from: https://www.whitehouse.gov/the-press-office/2013/02/12/presidential-policy-directive-critical-infrastructure-security-and-resil [Accessed: Feb. 2016].

[2] Olivares, D.E.; Mehrizi-Sani, A.; Etemadi, A.H.; Canizares, C.A.; Iravani, R.; Kazerani, M.; Hajimiragha, A.H.; Gomis-Bellmunt, O.; Saeedifard, M.; Palma-Behnke, R.; Jimenez-Estevez, G.A.; Hatziargyriou, N.D. Trends in microgrid control. IEEE Transactions on Smart Grid. 2014;5(4):1905–1919.

[3] Guerrero, J.M.; Vasquez, J.C.; Matas, J.; de Vicuña, L.G.; Castilla, M. Hierarchical control of droop- controlled AC and DC microgrids–A general approach toward synchronisation. IEEE Transactions on Industrial Electronics. 2011;58(1):158–172.

[4] Bidram, A.; Davoudi, A. Hierarchical structure of microgrids control system. IEEE Transactions on Smart Grid. 2012;3(4):1963–1976.

[5] Dragicevic, T.; Lu, X.; Vasquez, J.C.; Guerrero, J.M. DC microgrids—Part II: A review of power architectures, applications, and standardization issues. IEEE Transactions on Power Electronics. 2016;31(5):3528–3549.

[6] Elsayed, A.; Mohamed, A.; Mohammed, O. DC microgrids and distribution systems: An overview. Electric Power Systems Research. 2015;119:407–417.

[7] Balog, R.S.; Krein, P.T. Bus selection in multibus DC microgrids. IEEE Transactions on Power Electronics. 2011;26(3):860–867.

[8] Majumder, R. A hybrid microgrid with DC connection at back to back converters. IEEE Transactions on Smart Grid. 2014;5(1):251–259.

[9] Nejabatkhah, F.; Li, Y.W. Overview of power management strategies of hybrid AC/DC microgrid. IEEE Transactions on Power Electronics. 2015;30(12):7072–7089.

[10] Yu, X.; She, X.; Zhou, X.; Huang, A.Q. Power management for DC microgrid enabled by solid-state transformer. IEEE Transactions on Smart Grid. 2014;5(2):954–965.

[11] Mohamed, A.; de Cossio, F.C.; Ma, T.; Farhadi, M.; Mohammed, O. Operation and protection of photovoltaic systems in hybrid AC/DC smart grids. IECON 2012—38th Annual Conference on IEEE Industrial Electronics Society. 2012, Montreal; 1104–1109.

[12] Li, W.; He, X. A family of isolated interleaved boost and buck converters with winding-cross-coupled inductors. IEEE Transactions on Power Electronics. 2008;23(6):3164–3173.

[13] Elshaer, M.; Mohamed, A.; Mohammed, O. Grid connected DC distribution system for efficient integration of sustainable energy sources. IEEE/PES Power Systems Conference and Exposition (PSCE). 2011, Phoenix, AZ; 1–9.

[14] Mohamed, A.; Elshaer, M.; Mohammed, O. Bi-directional AC-DC/DC-AC converter for power sharing of hybrid AC/DC systems. 2011 IEEE Power and Energy Society General Meeting. 2011, San Diego, CA; 1–8.

[15] Dragicevic, T.; Guerrero, J.M.; Vasquez, J.C.; Skrlec, D. Supervisory control of an adaptive-droop regulated dc microgrid with battery management capability. IEEE Transactions on Power Electronics. 2014;29(2):695–706.

[16] Diaz, N.L.; Dragicevic, T.; Vasquez, J.C.; Guerrero, J.M. Intelligent distributed generation and storage units for dc microgrids—a new concept on cooperative control without communications beyond droop control. IEEE Transactions on Smart Grid. 2014;5(5):2476–2485.

[17] Mohamed, A.; Salehi, V.; Mohammed, O. Reactive power compensation in hybrid AC/DC networks for smart grid applications. 2012 3rd IEEE PES Innovative Smart Grid Technologies Europe (ISGT Europe). 2012, Berlin; 1–6.

[18] Salehi, V.; Mohamed, A.; Mazloomzadeh, A.; Mohammed, O. Laboratory-based smart power system, part II: Control, monitoring, and protection. IEEE Transactions on Smart Grid. 2012;3(3):1405–1417.

IntechOpen